

Electrodeposited cobalt films: hcp versus fcc nanostructuring and magnetic properties

J.L. Bubendorff^a, C. Mény^b, E. Beaurepaire, P. Panissod, and J.P. Bucher

Institut de Physique et Chimie des Matériaux de Strasbourg (IPCMS), Université Louis Pasteur, 23 rue du Loess, 67037 Strasbourg Cedex, France

Received 29 February 2000 and Received in final form 3 July 2000

Abstract. The crystallographic structure and morphology of electrodeposited cobalt films on Au(111) is found to be very sensitive on the electrolyte pH value and on the overpotential applied during deposition. The samples, 2 to 500 nm thick, were characterized by nuclear magnetic resonance (NMR), atomic force microscopy (AFM) and electron diffraction. The latter technique shows that the Co films grow in registry with the gold underlayer, reproducing the Au(111) texture. During the first stage of growth and depending on overpotential and pH value, either continuous hcp Co films or hcp Co islands are formed. Only the latter growth mode leads to an out of plane magnetization with 100% of remanence. Increasing the thickness, fcc Co becomes the prevailing phase. Eventually the fcc to hcp ratio saturates at the same value regardless the overpotential. The thickness for which the equilibrium fcc to hcp ratio is obtained as well as the sample structure and morphology before saturation, depend strongly on the overpotential value. In any case, the predominance of the fcc Co phase leads to an in plane magnetization of the thick samples. This study opens up new opportunities of engineering the properties of electrodeposited cobalt films.

PACS. 75.70.-i Magnetic films and multilayers – 81.15.Pq Electrodeposition, electroplating – 76.60.-k Nuclear magnetic resonance and relaxation

1 Introduction

Magnetic films and multilayers are the focus of much attention motivated mainly by their wide range of applications as magnetic data storage devices and sensors. However, the bulk of the work has been done on samples built by physical means of deposition such as molecular beam epitaxy or sputtering [1]. The electrochemical ways of deposition [2–9] are an interesting alternative to these techniques because they are easier to handle and much cheaper. Although the study of magnetic and transport (giant magnetoresistance) properties of these materials has just begun, there are already examples where properties similar to those obtained for vacuum grown samples are observed [2–8]. In addition, electrochemical routes of preparation allow to grow structures with high aspect ratio which are not possible to obtain by MBE deposition followed by lithographic processes [5,6]. Nevertheless, electrochemical techniques share with the other techniques a high sensitivity of the samples magnetic and transport properties on their crystallographic

and chemical structure. Therefore, a detailed structural characterization of the electrodeposited films is of prime importance to understand the properties of the samples.

Recently, we have evidenced the tremendous influence of the overpotential (a measure for the supersaturation) on the growth and consequently on the magnetic properties of ultrathin electrodeposited cobalt films [8,10]. We succeeded in stabilizing a perpendicular orientation of the magnetization in the thickness range of 2 to 7 monolayers of cobalt, in the high overpotential limit. This magnetic configuration is important for magneto-optic data storage applications and could be achieved, up to now, on vacuum deposited films only [11,12]. Due to the strong influence of the growth parameters on thin film magnetism, important effects are also anticipated for thicker films. Therefore, in this work we extend our previous study to thicker Co films from 2 nm to 500 nm. We show that the growth proceeds in different stages when the film thickness is increased. The proportion of fcc *versus* hcp phases and grain sizes change during growth and depend on the overpotential and pH. To our knowledge there is only one detailed study of the structure of electrodeposited cobalt films [13]. It was shown that on copper substrate either fcc or hcp cobalt was formed depending on the value of the pH and on the quality of the buffer solution.

^a Present address: Laboratoire de Microscopie Électronique et Tunnel, Université de Reims-Champagne-Ardennes, 21 rue Clement Ader, 51685 Reims Cedex 2, France

^b e-mail: Christian.Meny@ipcms.u-strasbg.fr

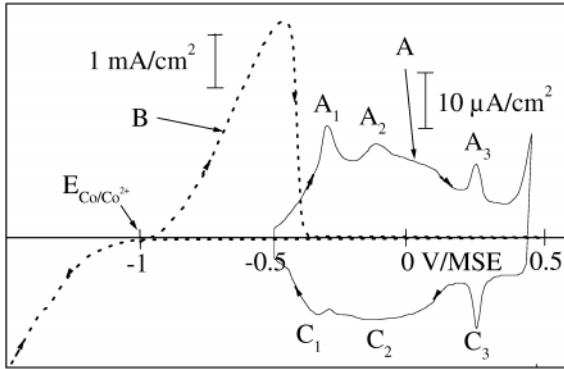


Fig. 1. Voltamogram (curve A) of a Au(111) electrode and dissolution peak of cobalt (curve B) in 0.6 M H_3BO_4 , 4×10^{-2} M CoSO_4 , 9×10^{-3} M CoCl_2 . Peaks A1, A2, C1 and C2 are a signature of the $\sqrt{3} \times 22$ reconstruction of the Au(111) surface. A3 and C3 are related to an order disorder transition of the adsorbed sulfate ions (see Ref. [18]).

2 Sample preparation

Electrodeposition was performed in a three electrode arrangement Pyrex cell (50 ml) under potentiostatic control. A mercury potassium sulfate electrode (MSE) was used as a reference, and a platinum wire as a counter electrode (CE), the working electrode (WE) being the substrate to be covered. Electrolyte solutions of $\text{CoSO}_4 \cdot 7\text{H}_2\text{O}$: 4×10^{-2} M, $\text{CoCl}_2 \cdot 6\text{H}_2\text{O}$: 9×10^{-3} M and H_3BO_3 : 0.65 M were prepared with reagent grade chemicals in bi-distilled water. This amount of H_3BO_3 leads to a solution with $\text{pH} = 4$. In order to keep the subsequent interpretation of magnetic properties as simple as possible, no additives (such as saccharine [14] or benzotriazole [15]) have been used. Nitrogen bubbling keeps the solution free of dissolved oxygen. $\text{pH} = 1$ is achieved by adding sulfuric acid (H_2SO_4) to the bath.

Gold substrates were prepared by vacuum evaporation of 100 nm thick gold films onto freshly cleaved mica substrates. Each sample was then flame annealed for a few seconds and quenched in ultra-pure water in order to remove any contaminants. This leads to (111) textured gold films with terraces 100 to 200 nm wide as verified by STM [16]. Electrodeposition of cobalt is only performed after a high quality Au(111) WE has been identified by its characteristic $\sqrt{3} \times 22$ reconstruction and de-reconstruction peaks in cyclic voltamograms (respectively A₁ and C₁ in Fig. 1) [17]. The voltamograms show also two other characteristic features of a Au(111) electrode in presence of sulfate ions [18]: two peaks, A₂ and C₂, corresponding to the adsorption and desorption of sulfate ions and two peaks, A₃ and C₃, corresponding to an order-disorder transition of the adsorbed sulfate monolayer [18]. The later operation is part of a typical electrodeposition experiment and is designed by the mention “test” in the diagram Figure 2. It guarantees a high reproducibility of the Au surface quality. Deposition proceeds, according to Figure 2, during t_d at a potential U inferior to

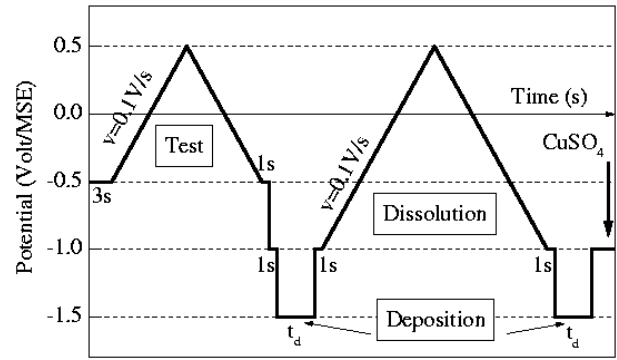


Fig. 2. Applied potential *versus* time for a cobalt electrodeposition experiment.

the Nernst potential of the Co/Co^{2+} couple $U_{\text{Co}/\text{Co}^{2+}}$ ($= -1.02$ V/MSE, potential quoted *versus* the MSE). During the deposition, the overpotential $\eta = |U - U_{\text{Co}/\text{Co}^{2+}}|$ measures the departure from the Nernst potential. We found the onset of Co deposition at $\eta = 0.13$ V. The films have been grown at $\eta = 0.18$ V and $\eta = 0.68$ V. Since reduction reactions other than metal deposition can not be fully avoided and since hydrogen release occurs at the selected potential U, the Faraday law does not give the best estimate of the amount of deposited cobalt. Therefore, the amount of deposited cobalt is measured before the final deposition during a dissolution step (Fig. 2). During this operation, the cobalt film fully dissolves into the solution. Figure 1 shows the dissolution peak (dotted line B). The area of the peak allows to quantify [19] the number of deposited cobalt atoms. In order to get the corresponding thickness in atomic layers (AL), we assumed a hcp (0001) or fcc (111) texture of the cobalt film (1.85×10^{15} atoms/cm² for a Co hcp (0001) or Co fcc (111) atomic layer). However, electrochemical techniques only give average values of the thickness over the entire probe surface. As a matter of fact, edge effects are always present. In order to avoid these effects, we covered the edges with an insulating, electrochemically inactive, varnish. The procedure described above allows to control the amount of deposited cobalt within 0.1 AL. Under these experimental conditions deposits with a purity comparable to the purity of MBE grown samples can be achieved [7], as verified by Rutherford Back Scattering.

Finally, except for the samples intended for AFM characterizations, a solution of CuSO_4 10^{-2} M has been added to the base solution in order to deposit a copper capping film. Since the Nernst potential of Cu is -0.6 V/MSE (higher than the one of Co) it is easy to choose a Cu deposition potential for which the Co layer is stable, namely -1.0 V/MSE. Hence, an efficient 6 nm thick copper film is formed within three minutes. Dissolution experiments clearly show that Co only desorbs after complete desorption of Cu. This is a good test to check the ability of Cu to fully cover the Co film surface. Nevertheless, after emersion, the efficiency of the Cu capping has been checked by X-ray Photoemission Spectroscopy (XPS). It has been

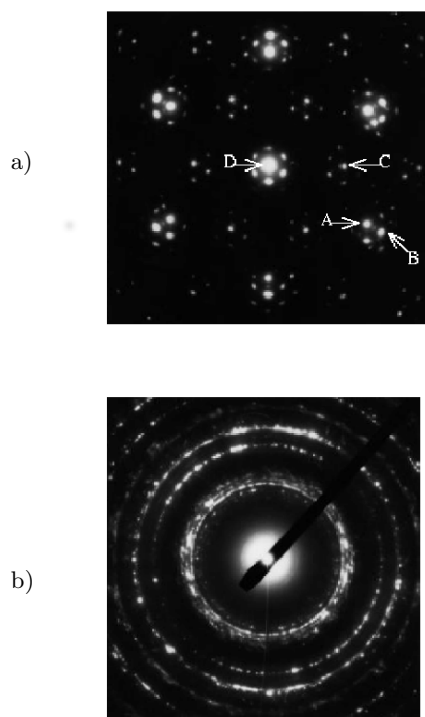


Fig. 3. Electron diffraction pattern of a Cu(6 nm)/Co(80 nm)/Au(111) sample grown at $\eta = 0.68$ V and pH = 4: electron beam size = 400 nm (a), electron beam size = 5 μm (b).

shown that all the Co atoms are in their metallic state. In the absence of the Cu film a 0.6 nm thick oxide film forms on the surface after exposure to ambient atmosphere.

3 Overpotential and pH dependent crystalline structure

3.1 Electron diffraction

Electron diffraction has been performed with a commercial 200 keV TOPCON microscope. After the mica substrates have been cleaved away, the samples were thinned by ion milling from the mica side. Figure 3a shows the diffraction pattern of a Cu(6 nm)/Co(80 nm)/Au(111) sample grown at $\eta = 0.68$ V. In this picture the electron beam was focused to a diameter of about 400 nm so that only one Au crystallite is involved in the diffraction pattern. The spot quoted D in Figure 3a corresponds to the direct beam. The six equivalent A type spots correspond to the diffraction from the (220) planes of Au. The six Co spots (B in Fig. 3a) can be indexed in both fcc and hcp Co structures as arising from the fcc (220) or hcp (11-20) planes. C can be attributed to hcp (10-10) or to fcc $1/3(422)$. The latter is normally forbidden in bulk fcc Co but can appear in case of twins within the Co layer thickness. Finally, the six satellites surrounding D, A and

C are due to double diffraction between Au and Co. The analysis of this diffraction pattern does not allow to determine whether the Co layer is in a fcc or hcp structure, but shows clearly that it grows as an oriented single crystal on the Au (111) crystallite with a fcc (111) or hcp (0001) growth direction. The lattice parameters measured from the diffraction patterns show that for this thickness, Co has its bulk lattice parameter. This is in agreement with the slight elongation of the Co spots (B). Indeed, it arises from a small misorientation of the Co in plane crystallographic axes with respect to the Au axes (about 3°). This enables to accommodate the lattice mismatch between the Co and gold layer.

A diffraction pattern taken with a wider electron beam diameter (5 μm) is shown in Figure 3b. The spots observed in Figure 3a become discontinuous rings because of the random in plane orientation of the Au (111) grains. No additional contribution to those already observed in Figure 3a can be distinguished. Similar diffraction patterns were observed on the samples grown at $\eta = 0.18$ V.

In summary, for both overpotentials the Co films grow in registry with the Au crystallites reproducing the texture of the underlying gold film. This is similar to what happens for films grown under UHV conditions [20,21]. The following AFM and NMR measurements provide more information about the topography and structure of the films.

3.2 AFM measurements

The evolution of the film surface topography with increasing cobalt thickness has been followed *ex situ* by Atomic Force Microscopy (AFM) on both series of samples ($\eta = 0.18$ V and $\eta = 0.68$ V) grown at pH = 4. The early growth stage ($t_{\text{Co}} < 6$ nm) has been analyzed quite in detail in a previous work [8,10]. It has been found that at low overpotential (0.18 V), the growing film follows the topography of the underlying gold substrate leading to nearly uniform film. At high overpotentials (0.68 V), on the contrary, the film is made of cobalt islands, 30 nm in diameter and 2 to 3 nm high. While at low overpotential the film grows laterally from step edges and defects, at high overpotential, cobalt islands nucleate all over the surface (progressive nucleation) and coalesce for $t_{\text{Co}} \approx 1.5$ nm [10]. Ultimately, at larger coverage, the latter growth mode leads to smoother films.

When the amount of deposited cobalt increases ($t_{\text{Co}} > 10$ nm), bigger and bigger 3D islands form at 0.18 V and the topography does not change anymore for $t_{\text{Co}} > 40$ nm. Figure 4b, for $t_{\text{Co}} = 60$ nm, shows that the surface of the sample is formed of grains with an average diameter of 240 nm and an average height of 50 nm. The scheme is very different in the case of films grown at an overpotential of 0.68 V. Due to the high supersaturation, small clusters that are continuously formed on the surface, start to coalesce from the beginning of growth, forming a nearly uniform and flat film, the topography stays unchanged up to $t_{\text{Co}} \approx 20$ nm. Increasing further t_{Co} , now leads to nucleation of bigger, almost spherical, cobalt clusters.

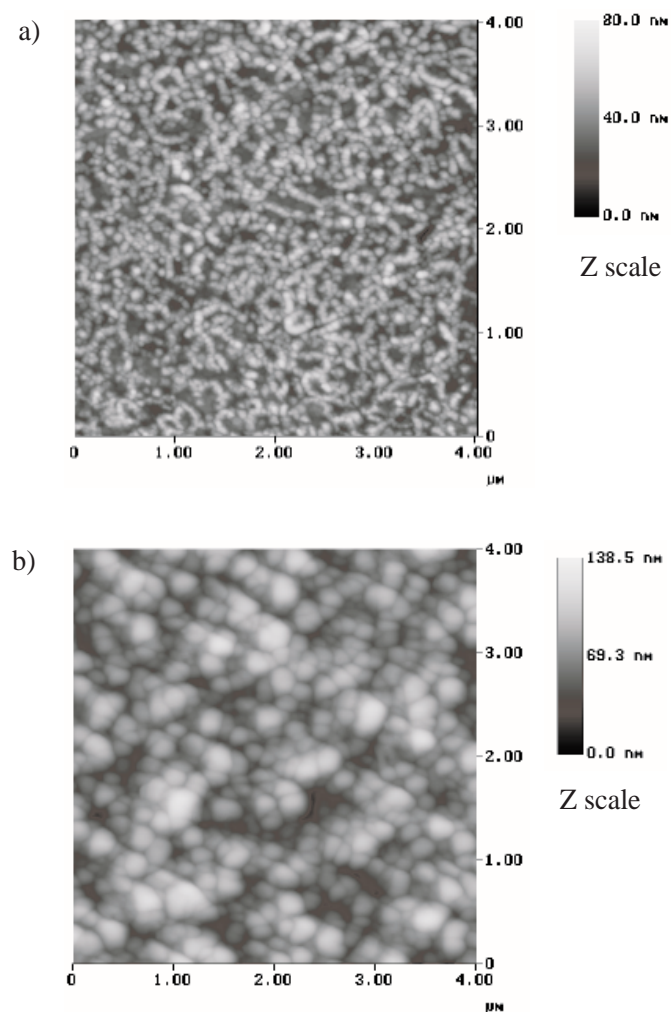


Fig. 4. Tapping mode AFM images of Co(60 nm)/Au(111) at pH = 4 and two different overpotentials: $\eta = 0.68$ V (a), $\eta = 0.18$ V (b).

The image of Figure 4a, corresponding to $t_{\text{Co}} = 60$ nm, shows that the cobalt clusters, about 60 nm in diameter, tend to organize in chains or rings. The size of these features scales exactly with the terrace-width of the underlying Au (111) layer. Therefore, the cluster organization in chains and rings is likely to result from a decoration of the grain boundaries. Above $t_{\text{Co}} = 80$ nm, the free space between the chains is progressively filled by new cobalt islands until at $t_{\text{Co}} = 100$ nm cobalt clusters fully occupy the surface. Above this thickness, the surface topography remains unchanged.

The different regimes of surface topography can be summarized in terms of RMS roughness. Figure 5 shows the evolution of the RMS roughness with increasing cobalt thickness t_{Co} for both growth conditions. The low overpotential situation leads to a growth exponent $\beta = 0.5 \pm 0.1$. At high overpotential, the roughness first stays constant and then increases steeply from 10 nm to 100 nm corresponding to a growth exponent $\beta = 0.7 \pm 0.1$. This regime

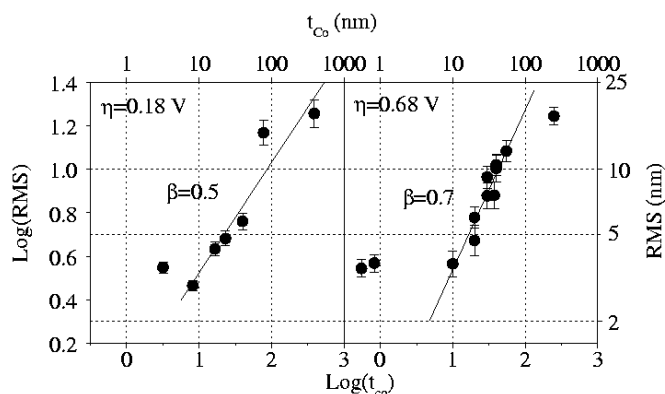


Fig. 5. RMS roughness as a function of Co thickness for two different overpotentials: $\eta = 0.18$ V (left), $\eta = 0.68$ V (right).

corresponds to the formation of chains and rings of clusters. Saturation of the RMS value sets in above 100 nm. The growth exponent $\beta = 0.5$, corresponding to films prepared at 0.18 V, are in good agreement with a model of random deposition of the adsorbed atoms [22]. The high value of $\beta = 0.7$, corresponding to deposits performed at 0.68 V, on the other hand, is quite unusual and can hardly be described by a simple model. It is certainly related to the growth mode characterized by monodisperse clusters forming chains and rings.

3.3 NMR measurements

Zero field ^{59}Co NMR spectra have been recorded with an automated broadband spectrometer [23]. For sake of sensitivity the samples were cooled down to 1.5 K for the 2 nm Co thick ones and down to 4.2 K for larger Co thickness. No NMR signal has been observed for the samples showing an out of plane component of their magnetization at thin Co thickness. We have investigated three series of samples. For the first one the Co thickness was kept about 2 nm (slightly above the Co thickness for which the magnetization becomes in plane) and we have studied the influence of the growth conditions (pH = 1 and 4 and overpotential $\eta = 0.18$ and 0.68 V) on the crystallographic structure of the Co layer. The two other series were intended to investigate the evolution of the structure of the Co layer with the increase of its thickness.

The spectra recorded on the 2 nm Co thick series are displayed in Figure 6. The full arrow shows the expected frequency of bulk hcp Co (~ 227 MHz) and the dashed one the frequency of bulk fcc Co (~ 217 MHz). It can be seen that both phases (fcc and hcp) are present whatever the growth conditions. Even if the hcp contribution dominates always over the fcc one, only the sample prepared at pH = 4 and $\eta = 0.68$ V shows a hcp line at the expected bulk hcp Co frequency. The small frequency shift observed on the other spectra can be explained by a small expansion of the Co lattice due to the large lattice mismatch between Au and Co or by defects in the hcp stacking. The influence of the growth conditions appears more clearly

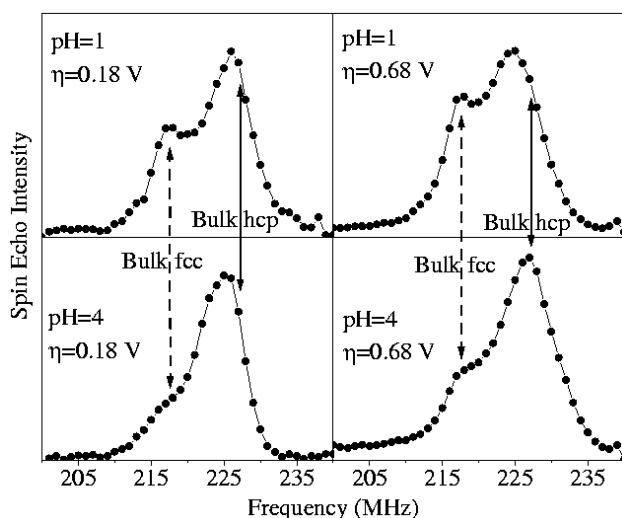


Fig. 6. NMR spectra of 2 nm thick cobalt films prepared under different conditions of pH and overpotential η .

on the fcc contribution. Indeed, it can be noticed that the fcc line is better resolved for the samples prepared at pH = 1 than for the samples prepared at pH = 4. This means that, at low pH, the fcc phase is well crystallized although it is not the majority phase here. Since the Co thickness corresponds to 10 atomic planes, it seems unlikely that such a well defined fcc line arises from a crossover from hcp to fcc (or the opposite) during the growth of the Co layer. Hence in the case of the pH = 1 samples there is certainly a simultaneous growth of large fcc and hcp Co grains from the beginning. For the pH = 4 samples the fcc line is much broader and the fcc contribution could be due to very small fcc grains or, as well, to stacking faults arising during the growth. The latter explanation seems to be ruled out by the following analysis of the spectra.

To obtain quantitative information about the amount of hcp and fcc phases, we have built a model to reproduce the experimental spectra. This model takes into account 4 lines (Fig. 7): two of them corresponding to the hcp (~ 227 MHz) and fcc (217 MHz) bulk contributions and the two others to the stacking faults (~ 220 MHz and ~ 223 MHz). As observed in bulk Co, the two lines for the stacking faults fall at about the same frequencies in hcp Co and in fcc Co. Hence, unless an additional assumption is made, we cannot attribute the corresponding intensities to one of the phases rather than to the other. Consequently we have assumed that the stacking faults are randomly distributed: it implies that, in a given phase, the intensities of the bulk line and the two defect lines obey a binomial law which depends only on the concentration of stacking faults in the phase (Fig. 7). Hence the model has three main parameters: 1) the fraction of hcp phase (in % of the total amount of bulk Co), 2) the concentration of stacking faults in the fcc phase (in % of the fcc fraction) and 3) the concentration of stacking faults in the hcp phase (in % of the hcp fraction). The secondary parameters are the positions and widths of each line but, in

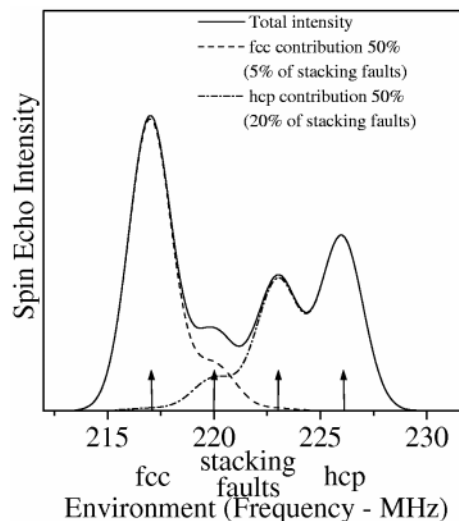


Fig. 7. Example of shape obtained with the model used to analyze the NMR spectra. The arrows show the position of the 4 lines involved in the model; from left to right: fcc bulk Co, the two stacking faults lines, hcp bulk Co. The stacking faults are assumed to be randomly distributed within the fcc and hcp fraction.

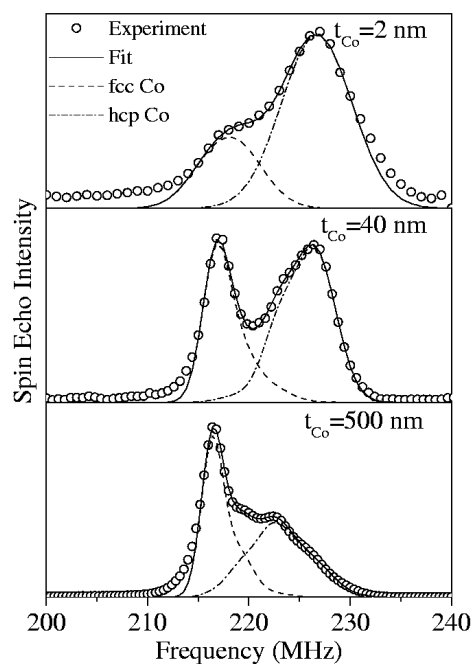
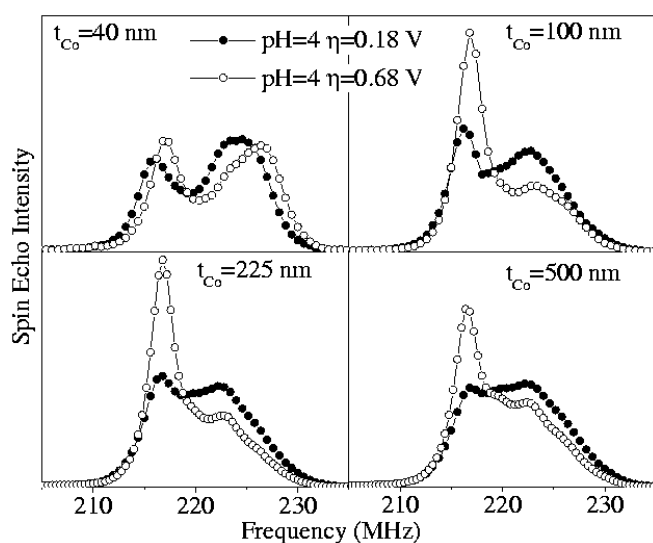


Fig. 8. NMR spectra of cobalt films deposited at $\eta = 0.68$ V and pH = 4. The lines show the decomposition into fcc and hcp contributions obtained with the model.

order to obtain a consistent description of the continuous structural evolution of the samples over the full range of Co thickness, we have fixed the positions and widths of the – less resolved – stacking fault lines. Only a limited shift of the resolved bulk lines has been allowed in order to fit the edges of the spectra. Figure 8 shows that this model enables to reproduce the NMR spectra for the whole range

Table 1. Respective contribution of hcp and fcc phases and their stacking faults for electrodeposited cobalt films; $t_{\text{Co}} = 2$ nm.

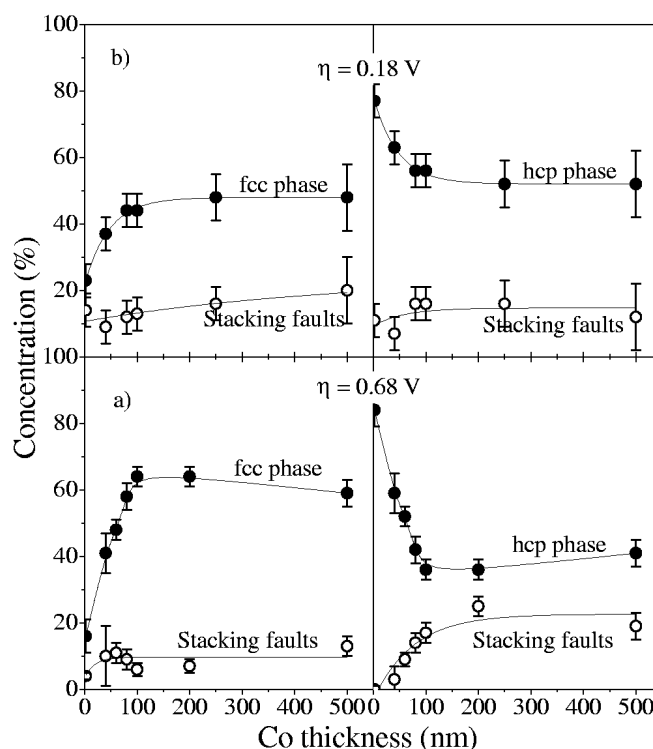
pH = 1, $\eta = 0.18$ V			pH = 1, $\eta = 0.68$ V		
% hcp Co	% faults in fcc	% faults in hcp	% hcp Co	% faults in fcc	% faults in hcp
66	20	0	64	20	4
pH = 4, $\eta = 0.18$ V			pH = 4, $\eta = 0.68$ V		
% hcp Co	% faults in fcc	% faults in hcp	% hcp Co	% faults in fcc	% faults in hcp
77	14	11	84	4	0

**Fig. 9.** Comparison of NMR spectra of electrodeposited cobalt films grown at same pH = 4 but two different overpotentials.

of Co thickness. This model has been checked against X-ray diffraction analyses in a study of Co/Mn multilayers [24]. Both techniques gave similar results.

The quantitative results obtained on the 2 nm Co thick series are given in Table 1. It confirms that the hcp phase dominates (the fcc fraction is only about 20%). The hcp phase is also slightly favored by pH = 4. The values obtained for the amount of stacking faults within each phase should be understood as indicative only since the stacking faults lines are not resolved (contrary to the case of the thick samples). Nevertheless, it can be noticed that the sample grown at pH = 4 and $\eta = 0.68$ V contains the smallest amount of stacking defects. It is also the only sample showing a hcp line exactly at the bulk hcp frequency. All the observations for this sample are consistent with a good crystalline quality of the dominant hcp phase while the minority fcc phase is contained in very small grains (broad line).

Since pH = 4 and $\eta = 0.68$ V give the best hcp structure, a series of samples with Co thickness ranging from 40 to 500 nm has been grown in order to investigate the dependence of the layer structure on Co thickness. Examples of spectra are shown in Figures 8 and 9. It can

**Fig. 10.** Evolution of the proportion of the fcc and hcp contributions and of their respective stacking faults as a function of cobalt thickness. pH = 4 and $\eta = 0.68$ V (a) and 0.18 V (b). Lines are guides for the eyes.

be seen that the fcc bulk contribution increases strongly and that the stacking faults contributions become rapidly larger than the bulk hcp contribution. The results of the quantitative analysis are summarized in Figure 10a. The fcc fraction increases steeply up to 100 nm. For this thickness 60% of the Co atoms are in an fcc structure. Above this thickness the hcp to fcc ratio stays almost constant up to 500 nm. The amount of stacking faults in the fcc phase is unchanged whatever the amount of fcc phase. On the contrary, while the amount of hcp Co decreases as a function of thickness, this phase becomes also more and more faulty as shown by the strong increase of the amount of stacking faults within this phase. Actually, for the thicker samples, most of the intensity that is attributed to hcp grains is contained in stacking faults. As mentioned above the amount of stacking faults attributed by the analysis

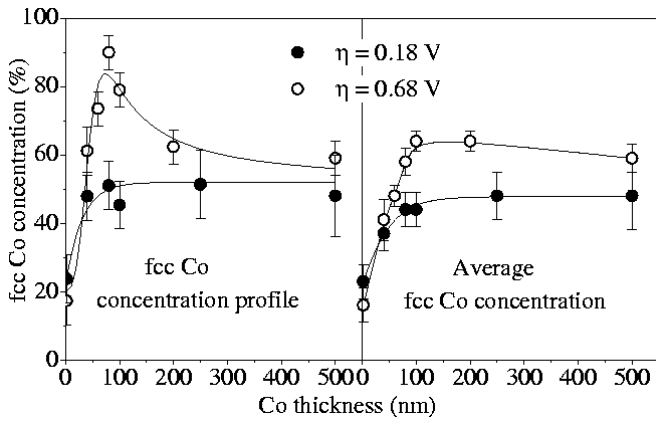


Fig. 11. Fcc Co concentration profile (left) determined from the thickness dependence of the average fcc Co concentration (right). Full circles: $\eta = 0.18$ V, open circles: $\eta = 0.68$ V. Lines are guides for the eyes.

to each phase depends on the prior assumption of a random distribution of these faults. We see here that a possible departure from randomness would mean that more stacking faults would be attributed to the fcc phase and, consequently the quoted fcc fraction is a lower limit. In summary, the growth conditions $\text{pH} = 4$ and $\eta = 0.68$ V initially favor a good hcp growth onto gold but, very soon, the fcc phase is favored for large thickness. Once the Co film thickness is thick enough to be insensitive to the substrate (Au in the present case) the Co structure reaches a kind of equilibrium between the two phases.

Finally we wanted to check if the behavior described in the previous paragraph was independent of the deposition rate (*i.e.* η). The comparison of the spectra obtained for samples with the same Co thickness, grown at the same pH but with two different overpotentials is given in Figure 9. It can be clearly seen that, for a low deposition rate ($\eta = 0.18$ V), the shape of the spectra evolves more slowly with increasing Co thickness and, for 100 nm, 60% (Fig. 10b) of the Co atoms are still in a hcp structure as compared to 40% for $\eta = 0.68$ V. For the thicker samples, the shape of the spectra is dominated by stacking faults and the quantitative analysis is very unstable against small changes in the line positions. Thus we cannot ascertain that the samples have reached an equilibrium between the two phases which are very faulty anyway.

The fcc and hcp Co concentrations given in Figure 10 correspond to average concentrations on the whole thickness of the sample. From those average concentrations it is possible to work out the concentration profile of fcc Co, *i.e.* the local fcc concentration between the thickness (t) and ($t + dt$). Indeed at a given thickness (t) the total amount of fcc Co can be written as :

$$tC_a(t) = \int_0^t C_1(x)dx \quad (1)$$

where $C_a(t)$ is the average fcc Co concentration at thickness (t) and $C_1(x)$ is the local fcc Co concentration at

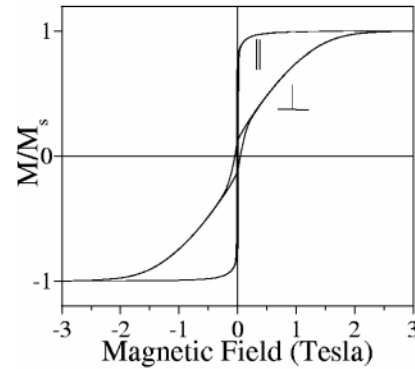


Fig. 12. In plane (\parallel) and out of plane (\perp) magnetization loop of a 100 nm thick sample grown at $\text{pH} = 4$ and $\eta = 0.18$ V.

thickness (x). With equation (1), by differentiation we find:

$$C_1(t) = C_a(t) + t \frac{d(C_a(t))}{dt} \quad (2)$$

$C_a(t)$ is known from the NMR analysis (Fig. 10) and a good estimate of $d(C_a(t))/dt$ is obtained by numerical derivation of the experimental $C_a(t)$ curves. The resulting fcc Co concentration profile is given in Figure 11 for both overpotentials. It can be seen that while for the samples deposited at $\eta = 0.18$ V the concentration profile is flat above 50 nm, for the samples prepared at $\eta = 0.68$ V, it goes through a maximum. Indeed, for a Co thickness of 80 nm almost pure fcc Co is deposited. Finally at 500 nm the local fcc Co concentration is close to 55% for both overpotentials. This analysis suggests that the same equilibrium between the fcc and hcp Co phases is achieved whatever the overpotential.

4 Magnetization measurements and discussion

The AFM and NMR measurements have shown that the morphology and crystallographic structure of the Co films depend strongly on the growth conditions: pH and overpotential. The first part of this section will show the influence of morphology and crystallography on the ability to stabilize, below 1.5 nm of Co, an out of plane magnetization direction. The second part will focus on the thick samples ($40 \text{ nm} < t_{\text{Co}} < 500 \text{ nm}$)

The magnetization measurements of the thin Co films have been described to some extent in references [8] and [10]. We recall that at $\text{pH} = 4$ and $\eta = 0.68$ V an out of plane magnetization with almost 100% of remanence has been obtained for Co thickness ranging from 3 to 7 AL. Other growth conditions lead to in plane magnetization or only to a weak out of plane component of the magnetization. In reference [10], the effective

anisotropy was analyzed as the sum of 3 terms: a volume term including magnetocrystalline anisotropy and magnetostriction, an interface term (accounting for Co/Au and Co/Cu interfaces) and a shape anisotropy term. The volume anisotropy was much stronger for the samples grown at high overpotential than for the samples grown at low overpotential (even stronger than the Co bulk one). This is consistent with both NMR and AFM analysis. As shown in Table 1, pH = 4 and $\eta = 0.68$ V are the growth conditions with the largest hcp to fcc Co ratio. They are also the only ones giving rise to a hcp Co line at exactly the expected bulk frequency. The good quality of the hcp structure which results in a strong magnetocrystalline anisotropy explains, at least partly, the large volume anisotropy obtained at high overpotential. Finally it has to be noticed that the out of plane magnetization vanishes at the Co thickness for which the Co islands coalesce, as seen by AFM [10]. This suggests that, even with a large volume anisotropy, the ability to achieve an out of plane magnetization is mainly driven by the shape anisotropy of the Co islands.

The magnetic properties of the thick films exhibit the same behavior regardless the overpotential. An example of magnetization loop is given in Figure 12. It can be seen that the magnetization remains mainly in plane. Even if an island growth is also observed between 10 and 100 nm at high overpotential, the fcc structure of the Co grains does not allow the magnetization to be out of plane. The origin of the fcc structure of the Co grains is to be found in the shape of the grains. Indeed, the large surface to volume ratio of the almost spherical grains observed in Figure 4a favors the fcc phase of Co by decreasing their surface energy. The fcc phase dominates over the hcp phase until the surface is filled up with Co grains. Then, above 200 nm, the fcc to hcp ratio reaches an equilibrium (55%, Fig. 11). At low overpotential the Co islands are more extended (Fig. 4b). This morphology is more efficient in stabilizing the Co hcp phase and therefore the fcc to hcp ratio reaches the equilibrium value as early as 40 nm of Co is deposited. Even if the morphology and structure of the samples depend strongly on the overpotential value, the large fcc Co fraction leads, whatever the overpotential, to a reduced magnetocrystalline anisotropy. Therefore it does not allow the nucleation of perpendicularly magnetized domains as in thick vacuum grown hcp Co films [25].

5 Conclusion

Using characterization techniques like electron diffraction AFM and NMR we have correlated the structure, morphology and magnetic properties of electrodeposited Co films with their growth conditions (pH and overpotential). The films grow in registry with the Au (111) underlayer regardless the growth conditions and the Co thickness. To stabilize, at small Co thickness, an out of plane magnetization, an island growth of well crystallized hcp Co is needed. Such a growth mode is favored by a pH

value of 4 and a high overpotential. Other growth conditions lead to continuous films containing a larger fraction of fcc Co. Increasing the Co thickness the fraction of hcp Co decreases strongly and eventually the fcc to hcp ratio reaches an equilibrium (55%). The Co thickness for which the equilibrium regime is obtained depends on the overpotential values (40 nm at low overpotential and 200 nm at high overpotential). The large fraction of fcc Co leads to an in plane magnetization of the samples for both overpotentials.

Even if the characterization techniques used in this study do not allow to determine whether the fcc and hcp Co fractions are included in a single cluster or are separated in different clusters, there are, nevertheless, two growth regimes in which the structure of the Co grains is well defined. At low Co thickness (≤ 2 nm) and whatever the growth conditions, the narrow fcc Co NMR line is the fingerprint of well crystallized grains. Therefore it can only arise from pure fcc clusters since the thickness of the sample is too thin to allow pure fcc and hcp Co phases to develop within a single cluster. The second well defined regime is achieved for the samples grown at pH4 and large overpotential. In the 70 to 110 nm thickness range almost pure fcc Co is deposited. In opposition, at low overpotential the fcc Co concentration increases smoothly, and therefore the fcc and hcp Co phases are likely to be included in each cluster. Even if a better understanding of the electrodeposition processes is needed, the variety of growth regimes observed in this study opens up new opportunities of engineering the properties of electrodeposited cobalt films

The authors would like to thank D. Raiser for performing the RBS measurements, J. Hommet for XPS measurements, G. Ehret, V. Pierron-Bohnes, and G. Wurtz for electron diffraction and R. Poinot for magnetic measurements

References

1. See for instance B. Heinrich, J.A.C. Bland, *Ultrathin Magnetic Structures I and II*, (Springer, Berlin, 1994).
2. M. Alper, K. Attenborough, V. Baryshev, R. Hart, D.S. Lashmore, W. Schwarzacher, *J. Appl. Phys.* **75**, 6543 (1994).
3. S.K.J. Lenczowski, C. Schönenberger, M.A.M. Gijs, W.J.M. de Jonge, *J. Magn. Mater.* **148**, 455 (1995).
4. N. Lebbad, J. Voiron, B. Nguyen, E. Chainet, *Thin Solid Films* **275**, 216 (1996).
5. A. Blondel, J.P. Meier, B. Doudin, J.-Ph. Ansermet, *Appl. Phys. Lett.* **65**, 3019 (1994).
6. L. Piraux, J.M. George, J.F. Despres, C. Leroy, E. Ferain, R. Legras, K. Ounadjela, A. Fert, *Appl. Phys. Lett.* **65**, 2484 (1994).
7. W. Schindler, J. Kirschner, *Phys. Rev. B* **55**, R1989 (1997).

8. J.L. Bubendorff, E. Beaurepaire, C. Mény, P. Panissod, J.P. Bucher, *Phys. Rev. B* **56**, R7120 (1997).
9. J.L. Bubendorff, J. Pflaum, E. Huebner, D. Raiser, J.P. Bucher, J. Pelzl, *J. Magn. Mag. Mat.* **165**, 199 (1997).
10. J.L. Bubendorff, E. Beaurepaire, C. Mény, J.P. Bucher, *J. Appl. Phys.* **83**, 7043 (1998).
11. C. Chappert, D. Renard, P. Beauvillain, J.P. Renard, J. Seiden, *J. Magn. Magn. Mater.* **54**, 795 (1986).
12. C. Chappert, P. Bruno, *J. Appl. Phys.* **64**, 5736 (1988).
13. H.L. Gaigher, N.G. van der Berg, *Electrochimica Acta* **21**, 45 (1976).
14. R.D. Fischer, *J. Electrochem. Soc.* **109**, 479 (1962).
15. M.J. Armstrong, R.H. Muller, *J. Electrochem. Soc.* **138**, 2303 (1991).
16. J.P. Bucher, L. Santesson, K. Kern, *Langmuir* **10**, 979 (1994).
17. J.M. Schott, H.S. White, *Langmuir* **8**, 1955 (1992).
18. O.M. Magnussen, J. Hageböck, J. Hotlos, R.J. Behm, *Faraday Discussion* **94**, 329 (1993).
19. J.L. Bubendorff, Ph.D. thesis, University Louis Pasteur of Strasbourg, France 1997.
20. C. Cesari, J.P. Faure, G. Nihoul, K. Le Dang, P. Veillet, D. Renard, *J. Magn. Mag. Mat.* **78**, 296 (1989).
21. B. Voigtländer, G. Meyer, N.M. Amer, *Phys. Rev. B* **44**, 10354 (1991); T.H. Gentner, F. Scheurer, T. Detzel, J.P. Bucher, *Thin Solid films* **275**, 58 (1996).
22. A.L. Barabasi, H.E. Stanley, *Fractal concets in surface growth* (Cambridge University Press, 1995).
23. P. Panissod, J.P. Jay, C. Mény, M. Wojcik, E. Jedryka, *Hyperfine Interac.* 97/98, 75 (1996).
24. V. Pierron-Bohnes, A. Michel, J.P. Jay, P. Panissod, *Mat. Res. Soc. Proc.* **528**, 169 (1998).
25. M. Hehn, S. Padovani, K. Ounadjela, J.P. Bucher, *Phys. Rev. B* **54**, 3428 (1996).